

Post-grazing dynamics of a vibro-impacting energy generator

Larissa Serdukova*, Rachel Kuske†, Daniil Yurchenko ‡

March 5, 2020

Abstract

The motion of a forced vibro-impacting inclined energy harvester is investigated in parameter regimes with asymmetry in the number of impacts on the bottom and top of the device. This motion occurs beyond a grazing bifurcation, at which alternating top and bottom impacts are supplemented by a zero velocity impact with the bottom of the device. For periodic forcing, we obtain semi-analytical expressions for the asymmetric periodic motion with a ratio of 2:1 for the impacts on the device bottom and top, respectively. These expressions are derived via a set of nonlinear maps between different pairs of impacts, combined with impact conditions that provide jump discontinuities in the velocity. Bifurcation diagrams for the analytical solutions are complemented by a linear stability analysis around the 2:1 asymmetric periodic solutions, and are validated numerically. For smaller incline angles, a second grazing bifurcation is numerically detected, leading to a 3:1 asymmetry. For larger incline angles, period doubling bifurcations precede this bifurcation. The converted electrical energy per impact is reduced for the asymmetric motions, and therefore less desirable under this metric.

1 Introduction

Energy Harvesting (EH) from ambient vibrations was proposed almost two decades ago as an attractive alternative to power supplies or as renewable sources of energy for rechargeable batteries. Since then the gaps in the linear theory of EH have been filled with different methods of energy conversion, based on single-degree-of freedom, multi-degree-of freedom and/or continuous (rods and beams) linear systems on the nano, micro and macro scales [1–5]. The excitement regarding the potential of linear EH systems has significantly decreased since then due to low energy densities of the linear devices, narrow bandwidth and high natural frequency in nano- and micro-scale systems, which are difficult to realize in many practical applications. These and other adverse factors lead to insufficient power output to power or recharge a battery. The deficiencies in the development of linear EH devices has slowed the proliferation of wireless sensors, particularly critical in the Internet of Things paradigm.

*School of Mathematics, Georgia Institute of Technology, Atlanta, GA 30313, USA. E-mail: larissa.serdukova@math.gatech.edu

†School of Mathematics, Georgia Institute of Technology, Atlanta, GA 30313, USA. E-mail: rachel@math.gatech.edu

‡IMPEE, Heriot-Watt University, Edinburgh, EH14 4AS, UK. E-mail: d.yurchenko@hw.ac.uk

The above limitations in the linear theory of EH have motivated wide-spread efforts on parametrically excited, nonlinear and non-smooth systems. The idea behind parametrically excited systems is the use of large system responses near instabilities, e.g. see [6–15], among others. Within the huge range of nonlinear EH systems, there are some particular themes of note; natural single-potential nonlinearities (classical continuous nonlinear systems like the Van-der-Pol or Duffing oscillator, a pendulum, etc. as in [16–22]), natural or imposed geometrical nonlinearities (systems with double, triple or multiple stable equilibria, as in [23–30]), systems with a nonlinear interaction such as flow-induced vibration systems (see [31–35] and references therein), and systems with strongly nonlinear or discontinuous nonlinearities like dry friction, piecewise discontinuity or vibroimpacts [36, 37]. It has been shown that the nonlinear mechanisms for EH are far more beneficial than linear ones. This observation follows from the typical structure of the response amplitude vs. forcing frequency or backbone curve, showing a wider bandwidth with higher response amplitude away from a main resonance frequency. However, the design and optimization of a nonlinear energy harvester is far more complex, with limited explicit analytical results, thus requiring extensive complementary experiments or numerics. The available approximation techniques can estimate the response within only a narrow range of parameters imposed by the mathematical assumptions necessary for the applied averaging procedure, typically based on a weakly nonlinear model with small forcing.

Vibro-impact systems have rich phenomenological behaviors, manifesting various nonlinear phenomena like bifurcations, grazing and chaos. These effects have been studied in deterministic and stochastic vibro-impact systems, as in [38–47] among others. The models of vibro-impact systems include piecewise linear stiffness [48, 49] as well as rigid barriers and instantaneous impacts leading to a velocity jump for inelastic impacts. EH devices that utilize vibro-impact dynamics as a main energy absorption mechanism were developed and studied in a number of publications [50–53]. While often such systems are limited to computational results only, certain settings allow an analytical or semi-analytical treatment when the motion is composed of a sequence of trajectories described (semi-)analytically. Such an approach translates the piecewise continuous behavior into a sequence of maps, amenable to analytical treatment [45]. This methodology has certain benefits since it allows bifurcation and stability analyses of various periodic regimes that may occur in the system. Of course, for more complex motions a series of maps is necessary, making these derivations more tedious and cumbersome.

Recently, [54] proposed a novel vibro-impact energy harvesting (VI-EH) device utilizing dielectric elastomeric (DE) membranes. There it was shown that the performance of such VI-EH depends strongly on the relationship between the excitation and device parameters, leading to various vibro-impact regimes with a low or high power output. The device consists of a forced cylinder with a ball moving freely inside of it, impacting DE membranes covering both ends of the cylinder. Each membrane is composed of the DE material sandwiched between two compliant electrodes, acting as a variable capacitance capacitor. Impact of the DE membrane by the ball influences its motion while deforming the membrane, leading to energy harvesting via the properties of variable capacitance. We characterize the motion of the VI-EH in terms of the ratio $n:m$ of impacts per period of the forcing, where n and m are the number of impacts against the bottom and top membrane, respectively. Here we restrict our attention to $m = 1$, as these types of solutions appear over significant parameter ranges when the cylinder is inclined.

The bifurcations and linear stability of the 1:1 periodic motion (two alternating bottom and top impacts per period) was investigated in [55], demonstrating the influence of parameters such as the length of the

cylinder, excitation parameters, and incline angle on this motion and the corresponding VI-EH power output. However, this study did not consider adjacent parameter regimes where $n:1$ periodic motions, period doubling bifurcation, and chaotic motion were observed numerically. In this paper we take a wider view to study semi-analytical solutions and stability conditions for 2:1 (three impacts per period) periodic motion, which has implications for the device's energy harvesting potential. A mechanical model and equations of motion of the VI-EH are described in Section 2, together with a review of the results from [55]. In Section 3 semi-analytical expressions for a 2:1 periodic motion are derived through three nonlinear maps, corresponding to the three impacts per period, combined with the impact conditions. A linear stability analysis for this motion is given in Section 4. The voltage output of the 2:1 periodic motion is shown in Section 5 and compared with that for the 1:1 periodic motion, together with comparisons of different metrics for the average energy available for harvesting. Finally, conclusions are drawn together with recommendations for the device design.

2 Previous results for the vibro-impacting energy harvester (VI-EH)

We give the equations of motion for the inclined VI-EH with two DE membranes for harvesting energy from ambient vibrations as developed in [54], as shown in the schematic of Figure 1. The cylinder of mass

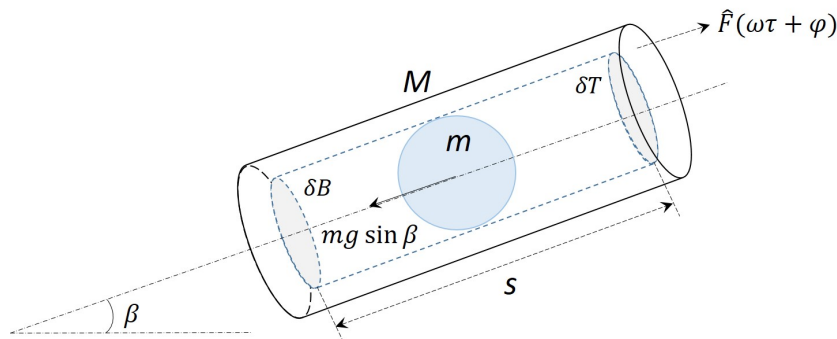


Figure 1: A mechanical model of a vibro-impact energy harvester adapted from [54].

M and length s is subject to a harmonic excitation $\hat{F}(\omega\tau + \varphi)$ with period $2\pi/\omega$. Then the position of its center $X(\tau)$ satisfies

$$\frac{\partial^2 X}{\partial \tau^2} = \frac{\hat{F}(\omega\tau + \varphi)}{M}. \quad (2.0.1)$$

Between impacts, the ball of mass m ($M \gg m$) rolls freely inside of the cylinder driven only by gravity ($g = 9.8 \text{ m/s}^2$ is the gravitational constant), with position x given by

$$\frac{\partial^2 x}{\partial \tau^2} = -G = -g \sin \beta, \quad (2.0.2)$$

until it collides with one of the membranes causing its deformation. At impact, the velocity of the ball changes in sign and magnitude according to

$$\left(\frac{\partial x}{\partial \tau}\right)^+ = -r \left(\frac{\partial x}{\partial \tau}\right)^- + (r+1) \frac{\partial X}{\partial \tau}. \quad (2.0.3)$$

Here r is the coefficient of restitution, and superscripts $-$ and $+$ indicate the velocities of the ball just before and after each impact, respectively. We assume that the velocity of the cylinder \dot{X} does not change with an impact for m negligible relative to M .

To track the dependence of periodic motions in terms of the parameters, it is valuable to use dimensionless equations of motion in terms of the relative variables. For this purpose we non-dimensionalize the original system (2.0.1), (2.0.2) with the substitutions

$$X(\tau) = \frac{\|\hat{F}\| \pi^2}{M\omega^2} \cdot X^*(t), \quad \frac{\partial X}{\partial \tau} = \frac{\|\hat{F}\| \pi}{M\omega} \cdot \dot{X}^*(t), \quad \tau = \frac{\pi}{\omega} \cdot t, \quad (2.0.4)$$

where $\|\hat{F}\|$ is an appropriately defined norm of the strength of the forcing \hat{F} and $\dot{}$ indicates the derivative with respect to t . Then the dimensionless equations of motion in terms of the relative position $Z(t)$ and velocity $\dot{Z}(t)$ are

$$\begin{aligned} Z &= X^* - x^*, & \dot{Z} &= \dot{X}^* - \dot{x}^* \\ \ddot{Z} &= \ddot{X}^* - \ddot{x}^* = F(\pi t + \varphi) + \frac{Mg \sin \beta}{\|\hat{F}\|} = f(t) + \bar{g}, \end{aligned} \quad (2.0.5)$$

where the non-dimensional forcing F has the unit norm, i.e. $\|F\| = 1$, and period 2. Then the impact condition (2.0.3) in terms of the non-dimensional relative variables for the j -th impact at time $t = t_j$ is

$$\begin{aligned} Z_j &= X^*(t_j) - x^*(t_j) = \pm \frac{d}{2}, \quad \text{for } x \in \partial B \text{ (} \partial T \text{) the sign is } + (-) \\ \dot{Z}_j^+ &= -r \dot{Z}_j^-, \end{aligned} \quad (2.0.6)$$

where $d = \frac{sM\omega^2}{\|\hat{F}\|\pi^2}$ is the length of the cylinder, ∂B and ∂T are the bottom and top membranes of the energy harvesting system.

By integrating (2.0.5) for $t \in (t_j, t_{j+1})$ and applying (2.0.6), we obtain the expressions for the relative velocity and displacement between two impacts

$$\dot{Z}(t) = -r \dot{Z}_j^- + \bar{g}(t - t_j) + F_1(t) - F_1(t_j), \quad (2.0.7)$$

$$Z(t) = Z_j^- - r \dot{Z}_j^- (t - t_j) + \frac{\bar{g}}{2} (t - t_j)^2 + F_2(t) - F_2(t_j) - F_1(t_j)(t - t_j), \quad (2.0.8)$$

where $F_1(t) = \int f(t)dt$ and $F_2(t) = \int F_1(t)dt$. In the following expressions, the superscripts " - " are omitted, since (2.0.7)-(2.0.8) are in terms Z^- and \dot{Z}^- only. Evaluating (2.0.7)-(2.0.8) at impact times $t = t_{j+1}$, we obtain equations defining the four basic nonlinear maps P_l , $l = 1, 2, 3, 4$ for the corresponding transitions between impacts,

$$\begin{aligned} P_1 & : (Z_j \in \partial B, \dot{Z}_j, t_j) \mapsto (Z_{j+1} \in \partial B, \dot{Z}_{j+1}, t_{j+1}), \\ P_2 & : (Z_j \in \partial B, \dot{Z}_j, t_j) \mapsto (Z_{j+1} \in \partial T, \dot{Z}_{j+1}, t_{j+1}), \\ P_3 & : (Z_j \in \partial T, \dot{Z}_j, t_j) \mapsto (Z_{j+1} \in \partial B, \dot{Z}_{j+1}, t_{j+1}), \end{aligned} \quad (2.0.9)$$

and similarly, for P_4 for the $\partial T \mapsto \partial T$ transition. Here we restrict our attention to P_1, P_2 and P_3 transitions, since only these play a role in the attracting 2:1 motion. The mathematical expressions for these maps take different forms depending on whether Z_j and Z_{j+1} are located on either ∂B or ∂T . Specifically, for $t = t_{j+1}$, (2.0.7) - (2.0.8) are given by

$$\dot{Z}_{j+1} = -r\dot{Z}_j + \bar{g}(t_{j+1} - t_j) + F_1(t_{j+1}) - F_1(t_j), \quad (2.0.10)$$

$$D_\ell = -r\dot{Z}_j(t_{j+1} - t_j) + \frac{\bar{g}}{2}(t_{j+1} - t_j)^2 + F_2(t_{j+1}) - F_2(t_j) - F_1(t_j)(t_{j+1} - t_j). \quad (2.0.11)$$

where $D_1 = D_4 = 0$, $D_2 = -d$ and $D_3 = d$.

In [55], the expressions (2.0.10)-(2.0.11) for the maps P_2 and P_3 over the time intervals (t_{k-1}, t_k) and (t_k, t_{k+1}) are combined with periodic and impact conditions to derive equations for the triples $(\dot{Z}_k, \varphi_k, \Delta t_k)$ corresponding to 1:1 periodic solutions. Throughout this paper $\Delta t_k = t_k - t_{k-1}$ for any k , and $\varphi_k = \text{mod}(\pi t_k + \varphi, 2\pi)$ is the phase shift of the k^{th} impact relative to that of the forcing $f(t)$. The resulting expressions provide the dependence of 1:1 motions on the combinations of the parameters d, r, \bar{g} and \hat{F} . A calculation of the energy output follows directly from these triples, based on the deformation of the membrane that depends explicitly on \dot{Z}_k . Given a constant input voltage, U_{in} , applied to the membranes, the change in charge Q across the capacitor is given by $\Delta Q = U\Delta C$, where C is its capacitance. The charge Q increases as the membrane's shape is restored, producing a higher voltage U_k at the k^{th} impact, with resulting energy to be harvested in terms of the difference, $U_k - U_{\text{in}}$, which we refer to as the output voltage.

In Figure 2 (a)-(d) we show the analytical and numerical results for the relative velocity at impact \dot{Z}_k and output voltage $U_k - U_{\text{in}}$ vs. d for the 1:1 periodic motion based on the results from [55]. In the top row, the different values of d follow from variation in s , while in the bottom row the different values of d follow from variation in \hat{F} . For decreasing values of d , the 1:1 period-2 motion loses stability via a sequence of period doubling bifurcations and eventually, for some parameter combinations, an apparently chaotic motion is observed for a window of values of d . For smaller values of d these 1:1 behaviors with longer period or chaos are displaced by asymmetric motions with multiple impacts of ∂B per period, that is, n:1 periodic motion. The analytical results corresponding to the branches for the 1:1 period-2 solutions are obtained both numerically and analytically in [55]. Branches corresponding to period doubled 1:1 solutions and chaotic behavior are obtained numerically. The analytical results shown for the 2:1 period-2 motion are obtained in Sections 3 and 4 below, where we restrict our analysis to the derivation of the 2:1 solutions and their linear stability. Numerical results are compared to these analytical solutions, and also

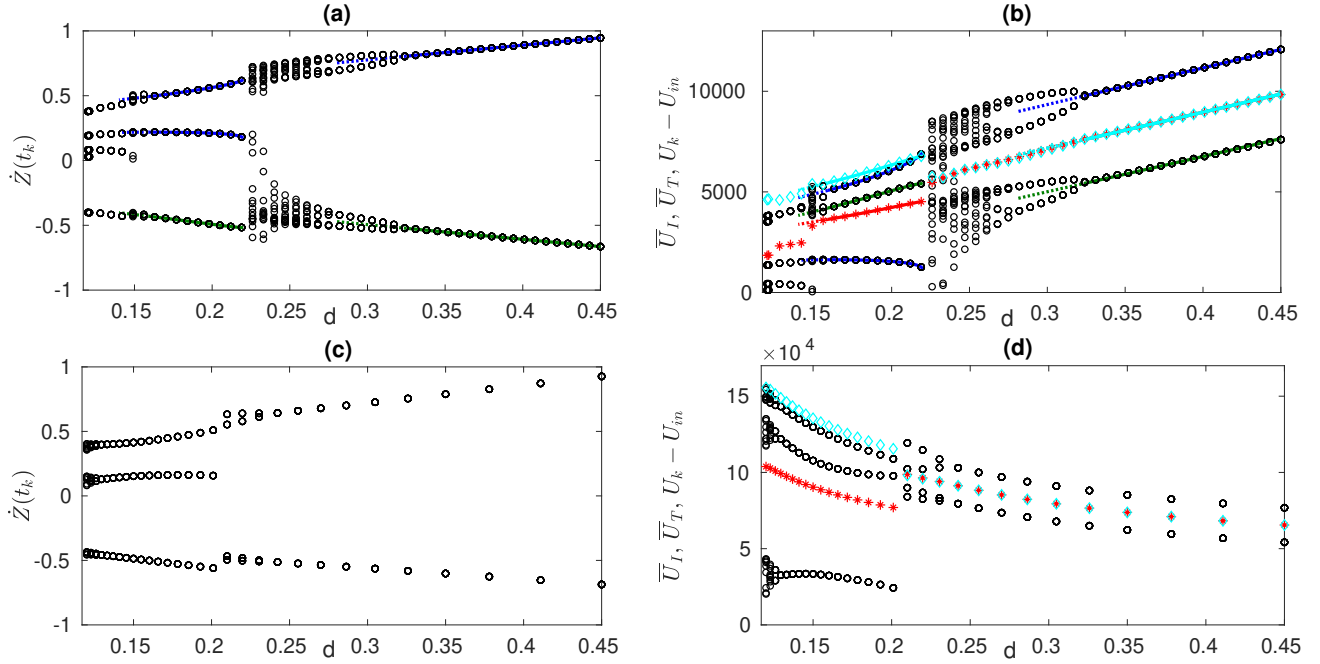


Figure 2: Numerical (open circles o 's, stars $*$'s, diamonds \diamond 's) and analytical stable/unstable (solid/dashed lines) values for impact velocities and output voltages for $\beta = \pi/3$. (a) Impact velocities (blue/green lines for bottom/top) for $0.19 < s < 0.72$, $\|\hat{F}\|=5$. The branches for the 2:1 solutions give, from top to bottom, \dot{Z} following the P_3, P_1, P_2 transitions. (b) Output voltage $U_k - U_{in}$ and average value of output voltage per impact \bar{U}_I (red stars) and per unit time \bar{U}_T (cyan diamonds) corresponding to \dot{Z} in (a). The branches for the 2:1 solutions give, from top to bottom, U_k following the P_3, P_2, P_1 transitions; (c)-(d) Impact velocity and output voltage for $s = 0.85$ with varying $\|\hat{F}\|$ between 6 and 22.

show additional bifurcations to $n:1$ periodic solutions, discussed further in Section 4. Analysis related to period doubling bifurcations, chaotic behavior, and grazing is left to future investigations.

Figure 2 (b) and (d) shows the corresponding output voltage $U_k - U_{in}$, for the same range of d as in (a) and (c). Two different averaged output voltages are also shown, average per impact \bar{U}_I and average per time unit \bar{U}_T , based on 30 (non-dimensionalized) time units in t ($\tau = 6$ sec.) for 1:1 motion and 20 time units in t ($\tau = 4$ sec.) for 2:1 motion. Note that the transition to different $n:1$ solutions corresponds to jumps in \bar{U}_I and \bar{U}_T , given the change in the nature of the periodic solution. The additional impacts have low velocity, following naturally from the fact that they are born via grazing bifurcations, at which $\dot{Z}_j = 0$ and $Z_j = d/2$. For example, at $d = d_{\text{graz}}$, $\dot{Z}_j = 0$ and $Z_j = \pm d/2$, and there is a transition to 2:1 motion for $d < d_{\text{graz}}$. Then the averaged per impact output voltage \bar{U}_I drops for increasing n . The averaged output per unit time \bar{U}_T is more complex, since the impact velocities following P_l for $l = 2, 3$ change with the addition of a low impact velocity from P_1 . The increase in output voltage is achieved through increased cylinder length s , with other parameters fixed, or by increasing the forcing strength keeping s constant, up to values of d where there are transitions to $n:1$ periodic motions. The impact velocity and output voltage in Figure 2 (c) and (d) are obtained for fixed $s = 0.85$ and the variable strength of the forcing $6 < \|\hat{F}\| < 22$, in contrast to (a) and (b) for which $\|\hat{F}\|=5$ is fixed and s varies for $0.118 < d < 0.448$. The nonlinear increase for $U_k - U_{in}$, \bar{U}_I and \bar{U}_T in (d) as d decreases is due to the inverse dependency of

$d = \frac{sM\omega^2}{\|\hat{F}\|\pi^2}$ on the strength of the forcing. Note that the forcing $\bar{g} = \frac{Mg \sin \beta}{\|\hat{F}\|}$ from the gravitational term in (2.0.5) is also inversely proportional to $\|\hat{F}\|$.

Figure 3 illustrates the typical transition from 1:1 to 2:1 families of solutions in the phase plane, via a sequence of period doublings, then grazing at a value of $d = d_{\text{graz}}$ at which $\dot{Z}_k = 0$ and $Z_k = d/2$ as shown in Figure 3 (b) and (f). From Figure 2 we see that 2:1 and other $n:1$ solutions persist for $d < d_{\text{graz}}$, with n increasing with decreasing d . To illustrate and compare the 1:1, 2:1 and 3:1 motions, Figure 4 shows the absolute displacements $X^*(t)$ of the top and bottom of the cylinder under an external force and the motion of the ball $x^*(t)$ in the cylinder. These show the number of impacts per period in each case.

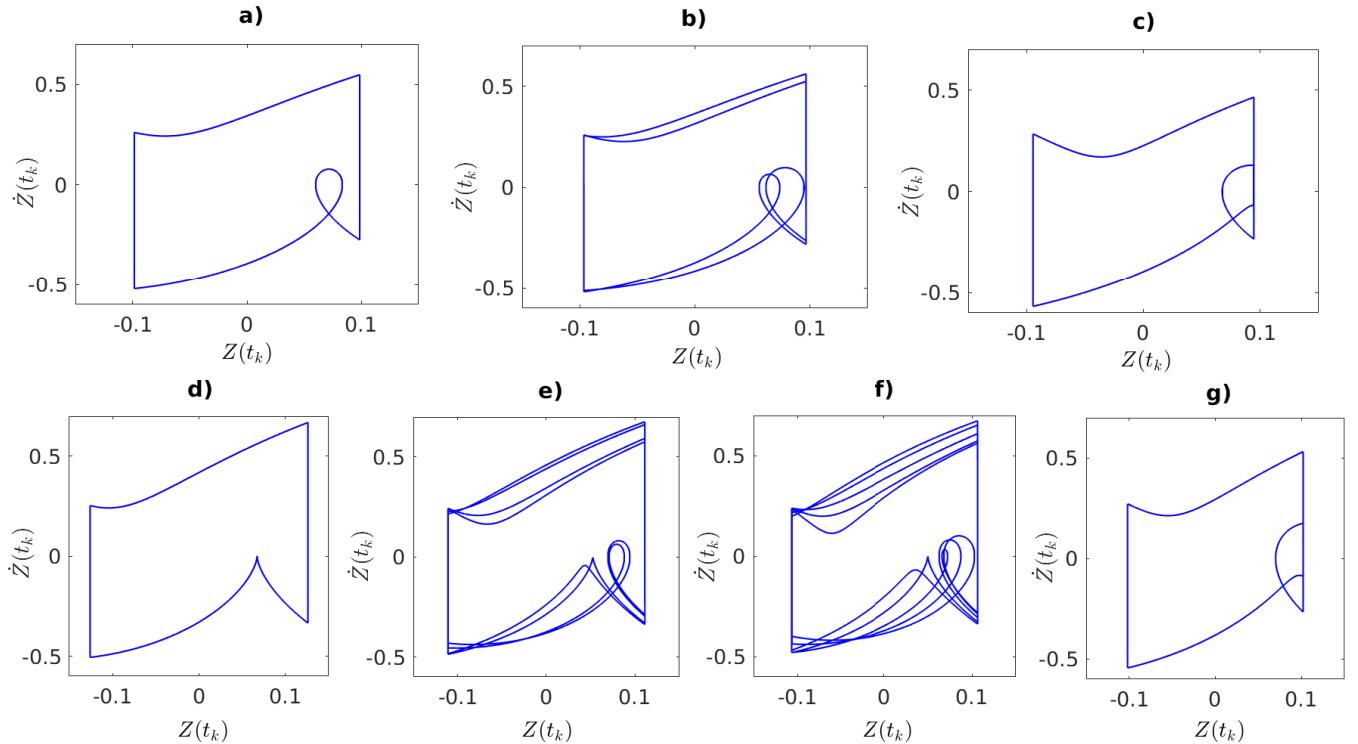


Figure 3: Phase portrait for initial relative position $Z(t_0) = d/2$, $M = 124.5$ g, $r = 0.5$. For (a)-(c) $\beta = \pi/2$, $\|\hat{F}\| = 61$ N and $\omega = 18\pi$ Hz; for (d)-(g) $\beta = \pi/6$, $\|\hat{F}\| = 5$ N and $\omega = 5\pi$ Hz. (a) 1:1 motion $d = 0.197$, $s = 0.316$, $\dot{Z}(t_0) = 0.5474$, $\varphi = 6.211$; (b) Grazing behavior for the 1:1 period-4 motion, with $d = 0.193$, $s = 0.309$, $\dot{Z}(t_0) = 0.561$, $\varphi = 6.229$; (c) 2:1 motion with $d = 0.189$, $s = 0.302$, $\dot{Z}(t_0) = 0.465$, $\varphi = 6.177$; (d) 1:1 motion $d = 0.252$, $s = 0.405$, $\dot{Z}(t_0) = 0.669$, $\varphi = 0.128$; (e) 1:1 period-8 motion $d = 0.222$, $s = 0.357$, $\dot{Z}(t_0) = 0.676$, $\varphi = 0.242$; (f) Grazing behavior of 1:1 period-10 motion $d = 0.213$, $s = 0.342$, $\dot{Z}(t_0) = 0.674$, $\varphi = 0.321$; (g) 2:1 motion $d = 0.204$, $s = 0.328$, $\dot{Z}(t_0) = 0.532$, $\varphi = 6.106$.

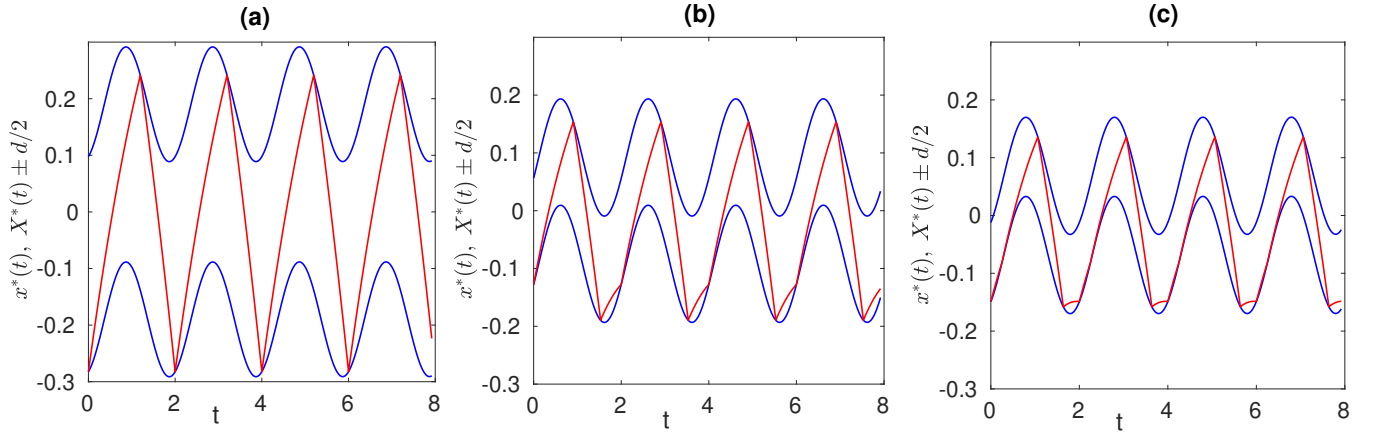


Figure 4: Time series of the period-2 absolute displacement of the capsule top and bottom $X^*(t) \pm d/2$ (blue lines) and the absolute ball displacement $x^*(t)$ (red line) for $t_0 = 0$ and $Z(t_0) = d/2$. (a) 1:1 motion for $d = 0.38$, $s = 0.61$, $\dot{Z}(t_0) = 0.8673$, $\varphi = 0.4217$; (b) 2:1 motion for $d = 0.184$, $s = 0.30$, $\dot{Z}(t_0) = 0.2164$, $\varphi = 1.21$; (c) 3:1 motion for $d = 0.137$, $s = 0.22$, $\dot{Z}(t_0) = 0.2059$, $\varphi = 0.6503$. For all figures $M = 124.5$ g, $r = 0.5$ and $\omega = 5\pi$ Hz.

3 Analytical expressions for periodic 2:1 motion

In this section we obtain analytical expressions for the parametric dependence of the 2:1 period-2 motion, using the maps P_1 , P_2 and P_3 for the sequence of impacts over the intervals Δt_j for $j = k, k + 1, k + 2$.

We derive equations for the quadruples $(\dot{Z}_k, \varphi_k, \Delta t_k, \Delta t_{k+1})$ corresponding to the 2:1 periodic solutions of (2.0.5) - (2.0.6), in terms of the parameters d , r and \bar{g} , with Δt_k and $\varphi_k = \text{mod}(\pi t_k + \varphi, 2\pi)$ as defined in Section 2. We focus on a 2:1 period- T motion with three impacts per period T of the forcing $f(t)$, so that

$$t_{k+3} = T + t_k, Z_k = Z_{k+3}, \text{ and } \dot{Z}_{k+3} = \dot{Z}_k. \quad (3.0.1)$$

The times for the transitions P_1 , P_2 and P_3 are defined as T_1 , T_2 and T_3 , with

$$\begin{aligned} T_1 &= \Delta t_k = t_{k+1} - t_k, & T_2 &= \Delta t_{k+1} = t_{k+2} - t_{k+1}, \\ T_3 &= \Delta t_{k+2} = t_{k+3} - t_{k+2}, & T &= T_1 + T_2 + T_3. \end{aligned} \quad (3.0.2)$$

The 2:1 period- T model is then described by the three maps P_1 , P_2 and P_3 from (2.0.10) and (2.0.11)

$$\begin{aligned} P_1 : (Z_k \in \partial B, \dot{Z}_k, t_k) &\mapsto (Z_{k+1} \in \partial B, \dot{Z}_{k+1}, t_{k+1}), \\ \dot{Z}_{k+1} &= -r\dot{Z}_k + \bar{g}T_1 + F_1(t_{k+1}) - F_1(t_k), \end{aligned} \quad (3.0.3)$$

$$0 = -r\dot{Z}_k T_1 + \frac{\bar{g}}{2} T_1^2 + F_2(t_{k+1}) - F_2(t_k) - F_1(t_k) T_1. \quad (3.0.4)$$

$$P_2 : (Z_{k+1} \in \partial B, \dot{Z}_{k+1}, t_{k+1}) \mapsto (Z_{k+2} \in \partial T, \dot{Z}_{k+2}, t_{k+2}),$$

$$\dot{Z}_{k+2} = -r\dot{Z}_{k+1} + \bar{g}T_2 + F_1(t_{k+2}) - F_1(t_{k+1}), \quad (3.0.5)$$

$$-d = -r\dot{Z}_{k+1}T_2 + \frac{\bar{g}}{2}T_2^2 + F_2(t_{k+2}) - F_2(t_{k+1}) - F_1(t_{k+1})T_2. \quad (3.0.6)$$

$$P_3 : (Z_{k+2} \in \partial T, \dot{Z}_{k+2}, t_{k+2}) \mapsto (Z_{k+3} \in \partial B, \dot{Z}_{k+3}, t_{k+3}),$$

$$\dot{Z}_{k+3} = -r\dot{Z}_{k+2} + \bar{g}T_3 + F_1(t_{k+3}) - F_1(t_{k+2}), \quad (3.0.7)$$

$$d = -r\dot{Z}_{k+2}T_3 + \frac{\bar{g}}{2}T_3^2 + F_2(t_{k+3}) - F_2(t_{k+2}) - F_1(t_{k+2})T_3. \quad (3.0.8)$$

We first use a number of substitutions to eliminate \dot{Z}_{k+1} , \dot{Z}_{k+2} from (3.0.3) - (3.0.8) and obtain four equations in terms of \dot{Z}_k , from which we obtain $(\dot{Z}_k, \varphi_k, \Delta t_k, \Delta t_{k+1})$.

By adding (3.0.3), (3.0.5), (3.0.7) and using the relationships $T = T_1 + T_2 + T_3$, and $F_1(t_{k+3}) = F_1(T + t_k) = F_1(t_k)$, we obtain

$$\dot{Z}_k = \frac{1}{1-r+r^2} \left[(r-1)\bar{g}T_1 - \bar{g}T_2 + (1-r)F_1(t_k) + rF_1(t_{k+1}) - F_1(t_{k+2}) + \frac{T\bar{g}}{r+1} \right]. \quad (3.0.9)$$

A second equation for \dot{Z}_k is obtained from (3.0.4)

$$\dot{Z}_k = \frac{1}{rT_1} [F_2(t_{k+1}) - F_2(t_k)] + \frac{1}{2r} [\bar{g}T_1 - 2F_1(t_k)]. \quad (3.0.10)$$

Substituting (3.0.3) into (3.0.6) yields a third expression for \dot{Z}_k

$$\dot{Z}_k = \frac{1}{r} [\bar{g}T_1 + F_1(t_{k+1}) - F_1(t_k)] - \frac{1}{r^2T_2} [d + F_2(t_{k+2}) - F_2(t_{k+1})] - \frac{1}{2r^2} [\bar{g}T_2 - 2F_1(t_{k+1})]. \quad (3.0.11)$$

Finally, adding (3.0.4), (3.0.6), (3.0.8) and using relationship $F_2(t_{k+3}) = F_2(T + t_k) = F_2(t_k)$ gives a fourth equation for \dot{Z}_k

$$\begin{aligned} \dot{Z}_k = & \frac{1}{r^3T_3 - r^2T_2 + rT_1} \left[\frac{\bar{g}}{2}(T_1^2 + T_2^2 + T_3^2) + F_1(t_k)(-r^2T_3 + rT_2 - T_1) \right] + \\ & + \frac{1}{r^3T_3 - r^2T_2 + rT_1} [F_1(t_{k+1})(r^2T_3 - rT_2 + rT_3 - T_2) + r^2\bar{g}T_1T_3 - r\bar{g}T_1T_2] + \\ & + \frac{1}{r^3T_3 - r^2T_2 + rT_1} [-r\bar{g}T_2T_3 - (1+r)T_3F_1(t_{k+2})]. \end{aligned} \quad (3.0.12)$$

Then we solve (3.0.9) - (3.0.12) to obtain $(\dot{Z}_k, \varphi_k, \Delta t_k, \Delta t_{k+1})$, using the Matlab function *vpsolve*. A specific choice of $f(t) = \cos(\pi t + \varphi)$ for which

$$F_1(t) = \frac{1}{\pi} \sin(\pi t + \varphi) \quad \text{and} \quad F_2(t) = -\frac{1}{\pi^2} \cos(\pi t + \varphi), \quad (3.0.13)$$

provides specifics for the equations for $(\dot{Z}_k, \varphi_k, \Delta t_k, \Delta t_{k+1})$. It is convenient to write the time intervals between impacts in terms of the parameters q and p , that capture the fractions of the period of forcing corresponding to each of the three impacts as follows,

$$T_1 = 2nq, \quad T_2 = 2np, \quad T_3 = 2n(1 - q - p), \quad \text{and} \quad T = 2n. \quad (3.0.14)$$

We take $n = 1$ for which the period is $T = 2$. Without loss of generality, we take $t_k = 0$, so $\varphi_k = \text{mod}(\varphi, 2\pi)$. Then the four equations (3.0.9) - (3.0.12) take the form of \dot{Z}_k as functions of φ , q , and p

$$\begin{aligned} \dot{Z}_k = & \frac{1}{1 - r + r^2} \left[2nq(r - 1)\bar{g} - 2np\bar{g} + \frac{1 - r}{\pi} \sin(\pi t_k + \varphi) + \frac{r}{\pi} \sin(\pi[t_k + 2nq] + \varphi) \right] + \\ & + \frac{1}{1 - r + r^2} \left[-\frac{1}{\pi} \sin(\pi[t_k + 2nq + 2np] + \varphi) + \frac{2n\bar{g}}{r + 1} \right], \end{aligned} \quad (3.0.15)$$

$$\dot{Z}_k = \frac{1}{\pi r} \left[n\pi q \bar{g} - \sin(\pi t_k + \varphi) - \frac{1}{2n\pi q} \cos(\pi[t_k + 2nq] + \varphi) + \frac{1}{2n\pi q} \cos(\pi t_k + \varphi) \right], \quad (3.0.16)$$

$$\begin{aligned} \dot{Z}_k = & \frac{1}{\pi r^2} [\sin(\pi[t_k + 2nq] + \varphi) + 2n\pi q r \bar{g} + r \sin(\pi[t_k + 2nq] + \varphi) - r \sin(\pi t_k + \varphi)] + \\ & + \frac{1}{\pi r^2} \left[\frac{1}{2n\pi p} \cos(\pi[t_k + 2nq + 2np] + \varphi) - \frac{1}{2n\pi p} \cos(\pi[t_k + 2nq] + \varphi) - n\pi p \bar{g} - \frac{\pi d}{2np} \right], \end{aligned} \quad (3.0.17)$$

$$\begin{aligned} \dot{Z}_k = & \frac{\sin(\pi t_k + \varphi)(-2nr^2(1 - p - q) + 2npr - 2nq)}{2nr^3(1 - p - q) - 2npr^2 + 2nqr} - \\ & - \frac{2n \sin(\pi[t_k + 2nq + 2np] + \varphi)(1 - p - q)(1 + r)}{2n\pi r^3(1 - p - q) - 2n\pi pr^2 + 2n\pi qr} \\ & + \frac{\sin(\pi[t_k + 2nq] + \varphi)(2nr^2(1 - p - q) - 2npr + 2nr(1 - p - q) - 2np)}{2nr^3(1 - p - q) - 2npr^2 + 2nqr} + \\ & + \frac{4n^2 r^2 \bar{g} q(1 - p - q) - 4n^2 \bar{g} r p q - 4n^2 \bar{g} r p(1 - p - q) + \bar{g}(2n^2 q^2 + 2n^2 p^2 + 2n^2(1 - p - q)^2)}{2nr^3(1 - p - q) - 2npr^2 + 2nqr}. \end{aligned} \quad (3.0.18)$$

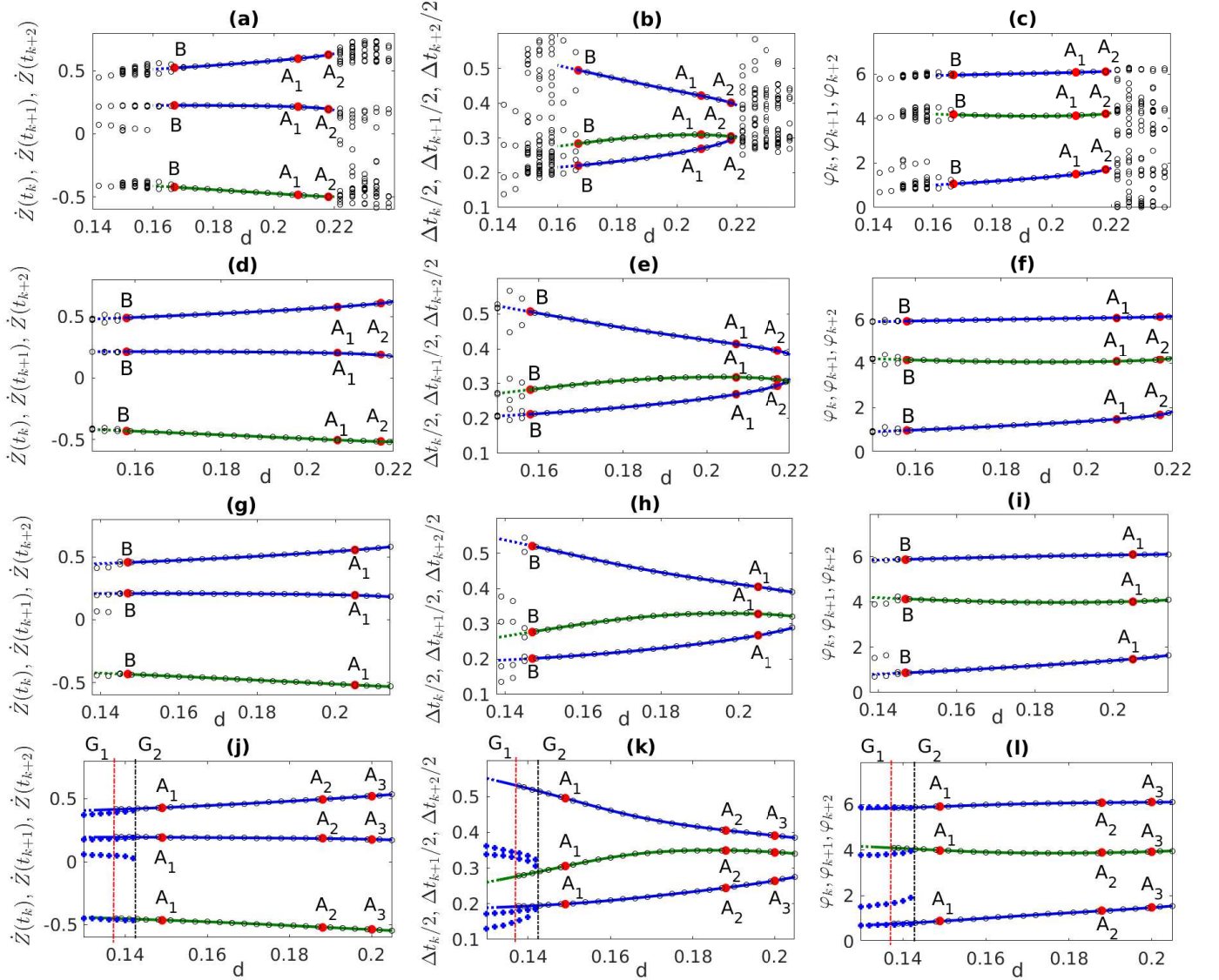


Figure 5: Blue and green lines show the analytical results for the 2:1 periodic solutions, with numerical results indicated by open circles. Solid (dashed) lines correspond to stable (unstable) analytical solutions. (a)-(c) Asymmetric branches of the period-2 solutions for $\beta = \pi/2$, and $0.27 < s < 0.37$; (d)-(f) Asymmetric branches of the period-2 solutions for $\beta = \pi/3$ and $0.25 < s < 0.37$; (g)-(i) Asymmetric branches of the 2-periodic solutions for $\beta = \pi/4$ and $0.22 < s < 0.33$; (j)-(l) Asymmetric branches of the period-2 solutions for $\beta = \pi/6$ and $0.22 < s < 0.33$. The vertical lines correspond to grazing bifurcations; $d = G_1$ (black) ($d = G_2$ (red)) for the transition from 3:1 to 2:1 (2:1 to 3:1) solutions with increasing (decreasing) d . In panels (a), (d), (g), (j) the branches for the 2:1 solutions give, from top to bottom, \dot{Z}_k at impacts following the P_3, P_1, P_2 transitions; in panels (b), (e), (h), (k) the branches for the 2:1 solutions give, from top to bottom, $\Delta t_j/2$ for the P_2, P_3, P_1 transitions; in panels (c), (f), (i), (l) the branches for the 2:1 solutions give, from top to bottom, the phase difference φ_k before the P_1, P_3, P_2 transitions. For all figures $M = 124.5$ g, $r = 0.5$, $\|\hat{F}\| = 5$ N and $\omega = 5\pi$ Hz.

Solving (3.0.15) - (3.0.18) for varying d , one gets the quadruples $(\dot{Z}_k, \varphi_k, \Delta t_k, \Delta t_{k+1})$ for 2:1 period-2 solutions. Then \dot{Z}_{k+1} is obtained from (3.0.3) and substitution of (3.0.3) into (3.0.5) gives the equation for \dot{Z}_{k+2}

$$\dot{Z}_{k+2} = r^2 \dot{Z}_k - r\bar{g}T_1 + \bar{g}T_2 + rF_1(t_k) - (1+r)F_1(t_{k+1}) + F_1(t_{k+2}). \quad (3.0.19)$$

Figure 5 shows the analytical solutions for these quadruples for different angles of incline β and compares them to the values obtained from numerical simulations of equations (2.0.5) - (2.0.6). The 2:1 period-2 solutions are stable only in the ranges of $0.167 < d < 0.22$ (a)-(c), $0.158 < d < 0.22$ (d)-(f), $0.147 < d < 0.214$ (g)-(i) and $0.1378 < d < 0.205$ (j)-(l). The stable 2:1 solutions, represented by the solid blue lines (impacts on ∂B) and green lines (impacts on ∂T) agree with the numerical solutions represented by black open circles. The unstable 2:1 solutions represented by dashed lines are also found analytically. The points A_1, A_2, A_3, B are the critical points that indicate a change in the type or stability or instability of the 2:1 solutions, based on the linear stability analysis. For the case of $\beta = \pi/6$ in the bottom row of Figure 5, vertical lines indicate the numerically detected grazing bifurcations at $d = G_1$ and $d = G_2$, corresponding to $Z_j = d/2$ and $\dot{Z}_j = 0$. There are two different values, since the bifurcation value differs depending on whether it is obtained from decreasing the parameter d , yielding a transition from a 2:1 period-2 solution to a 3:1 period-2 solution at $d = G_1$, or by increasing d , yielding a transition from 3:1 to 2:1 period-2 solutions at $d = G_2$. These results indicate a region of bi-stability for the 2:1 and 3:1 period-2 solutions, which we discuss briefly in Subsection 4.2.

4 Stability and Bifurcation of 2:1 period-2 motion

4.1 Linear stability analysis

The critical points A_j, B as shown in Figure 5 are obtained from a linear stability analysis around the quadruples $(\dot{Z}_k, \varphi_k, \Delta t_k, \Delta t_{k+1})$ corresponding to the asymmetric period-2 solutions. A complete review of this method can be found in [45, 46, 48].

Considering a small perturbation $\delta \mathbf{H}_k$ to the fixed point $\mathbf{H}_k^* = (t_k, \dot{Z}_k)$, we obtain the equation for $\delta \mathbf{H}_{k+3}$ linearized about $\delta \mathbf{H}_k = 0$,

$$\delta \mathbf{H}_{k+3} = DP(\mathbf{H}_k^*) \delta \mathbf{H}_k = DP_3(\mathbf{H}_{k+2}^*) \cdot DP_2(\mathbf{H}_{k+1}^*) \cdot DP_1(\mathbf{H}_k^*) \delta \mathbf{H}_k, \quad (4.1.1)$$

with

$$\begin{aligned} DP &= DP_3 \cdot DP_2 \cdot DP_1 = \\ &= \begin{bmatrix} \frac{\partial t_{k+3}}{\partial t_{k+2}} & \frac{\partial t_{k+3}}{\partial \dot{Z}_{k+2}} \\ \frac{\partial \dot{Z}_{k+3}}{\partial t_{k+2}} & \frac{\partial \dot{Z}_{k+3}}{\partial \dot{Z}_{k+2}} \end{bmatrix}_{\mathbf{H}_{k+2}=\mathbf{H}_{k+2}^*} \cdot \begin{bmatrix} \frac{\partial t_{k+2}}{\partial t_{k+1}} & \frac{\partial t_{k+2}}{\partial \dot{Z}_{k+1}} \\ \frac{\partial \dot{Z}_{k+2}}{\partial t_{k+1}} & \frac{\partial \dot{Z}_{k+2}}{\partial \dot{Z}_{k+1}} \end{bmatrix}_{\mathbf{H}_{k+1}=\mathbf{H}_{k+1}^*} \cdot \begin{bmatrix} \frac{\partial t_{k+1}}{\partial t_k} & \frac{\partial t_{k+1}}{\partial \dot{Z}_k} \\ \frac{\partial \dot{Z}_{k+1}}{\partial t_k} & \frac{\partial \dot{Z}_{k+1}}{\partial \dot{Z}_k} \end{bmatrix}_{\mathbf{H}_k=\mathbf{H}_k^*}. \end{aligned} \quad (4.1.2)$$

The entries $\frac{\partial t_{l+1}}{\partial t_l}, \frac{\partial t_{l+1}}{\partial \dot{Z}_l}, \frac{\partial \dot{Z}_{l+1}}{\partial t_l}, \frac{\partial \dot{Z}_{l+1}}{\partial \dot{Z}_l}$ for $l = k, k+1, k+2$ are given in A Appendix.

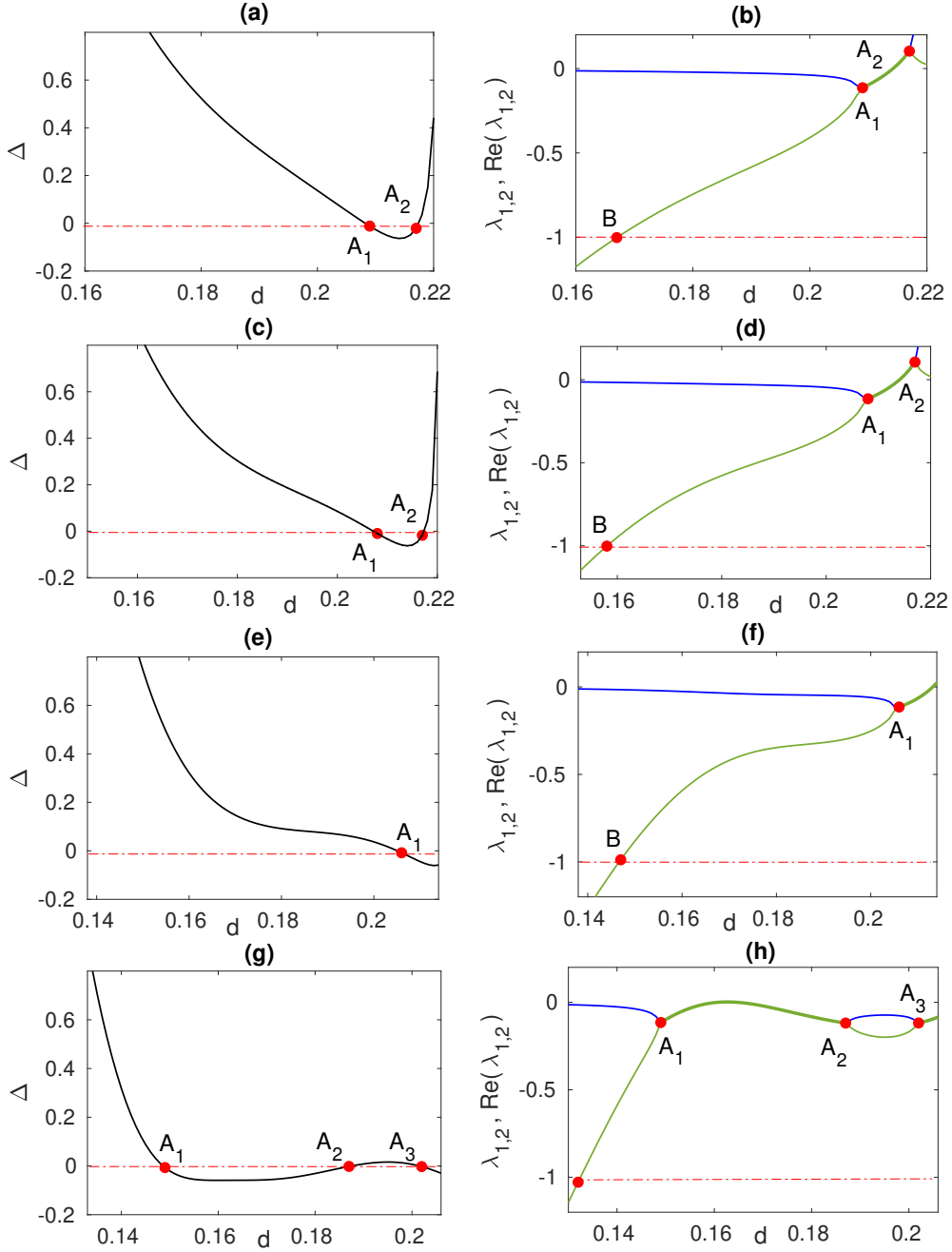


Figure 6: Graphs of Δ (left column), and eigenvalues from the linear stability analysis (right column), showing real eigenvalues $\lambda_{1,2}$ (blue and green thin lines) and real part of complex eigenvalues $\text{Re}\lambda_{1,2}$ (green thick line) to confirm types and stability of solutions. In (a) and (b) for $\beta = \pi/2$, $0.27 < s < 0.37$; in (c) and (d) for $\beta = \pi/3$ and $0.25 < s < 0.37$; in (e) and (f) for $\beta = \pi/4$ and $0.22 < s < 0.33$; in (g) and (h) for $\beta = \pi/6$ and $0.22 < s < 0.33$. The red dot-dashed lines for $\Delta = 0$ and $\lambda_{1,2} = -1$ represent boundaries of the stability criteria. The left-most red circle in (h) corresponds to $\lambda_j = -1$ from the stability analysis. For all figures $M = 124.5$ g, $r = 0.5$, $\|\hat{F}\| = 5$ N and $\omega = 5\pi$ Hz.

Using the trace $\text{Tr}(DP)$ (A.0.4) and determinant $\text{Det}(DP)$, the eigenvalues of the matrix DP in (4.1.2) are computed by

$$\lambda_{1,2} = \frac{\text{Tr}(DP) \pm \sqrt{\Delta}}{2},$$

$$\Delta = [\text{Tr}(DP)]^2 - 4\text{Det}(DP), \quad (4.1.3)$$

and shown in Figure 6. The corresponding stability and analytical bifurcation conditions as obtained from the linear stability analysis are described in Table 1 below.

Interval	Criteria	Stability
$d < d_B$	$\Delta > 0$ and $ \lambda_i > 1$	unstable node
$d_B < d < d_{A_1}, d_{A_2} < d < d_{A_3}$,	$\Delta > 0$ and $ \lambda_i < 1$	stable node
$d_{A_1} < d < d_{A_2}, d > d_{A_3}$	$\Delta < 0$ and $ \lambda_i < 1$	stable focus

Table 1: Conditions for stability as obtained from the linear stability analysis and shown in Figure 2, with, for example, d_{A_j} corresponding to the value of d at A_j .

In addition to these conditions, note that for smaller β , specifically $\beta = \pi/6$ in the last row of Figure 6, the linear stability analysis indicates an eigenvalue $\lambda_1 < -1$ for $d < .133$. This stability result is represented by a change from solid to dashed line for the analytical solutions shown in Figure 5 (j)-(l). However, the linear analysis does not capture the grazing bifurcations indicated by the dash-dotted vertical lines in Figure 5. Then, in practice, the grazing bifurcation for $d > .133$, rather than the local linearized behavior, drives the transition from 2:1 to 3:1 period-2 solutions. The values of d corresponding to grazing bifurcations are not included in Table 1, but instead discussed in Subsection 4.2 below.

If $\Delta < 0$, as shown for $d_{A_1} < d < d_{A_2}, d > d_{A_3}$ and in Figures 6 (a), (c), (e), (g), the eigenvalues of the matrix DP are two complex conjugates. Their corresponding real parts $\text{Re}(\lambda_i) = \text{Tr}(DP)/2$ are shown in Figures 6 (b), (d), (f), (h), depicted by the thick green line. In these intervals the 2:1 period-2 solution is a stable focus since the eigenvalues also satisfy the condition $|\lambda_i| = \sqrt{\text{Det}(DP)} < 1$.

If $\Delta > 0$ and $\min_{i=1,2}(\lambda_i) < -1$, as in $d < d_B$ ranges in Figures 6 (b), (d), (f), the period-2 solution is an unstable node. The corresponding critical point B is a period doubling bifurcation. For the angles of incline $\beta = \pi/2$ and $\beta = \pi/3$ the stability behavior of the periodic motion is very similar revealing the predominance of node stability in the observed range of d and having critical points of the same type: B period doubling bifurcation, A_1 node/focus inflection and A_2 focus/node inflection. For smaller β , the qualitative behavior of the 2:1 period-2 solutions changes; specifically, grazing bifurcations drive the transition to 3:1 period-2 solutions for larger values of d as compared with other critical values obtained from the linear stability analysis. We note that grazing bifurcations of the 2:1 period-2 solutions are observed for larger values of β as well. They are not shown here since they occur for values of $d < d_B$ in those cases.

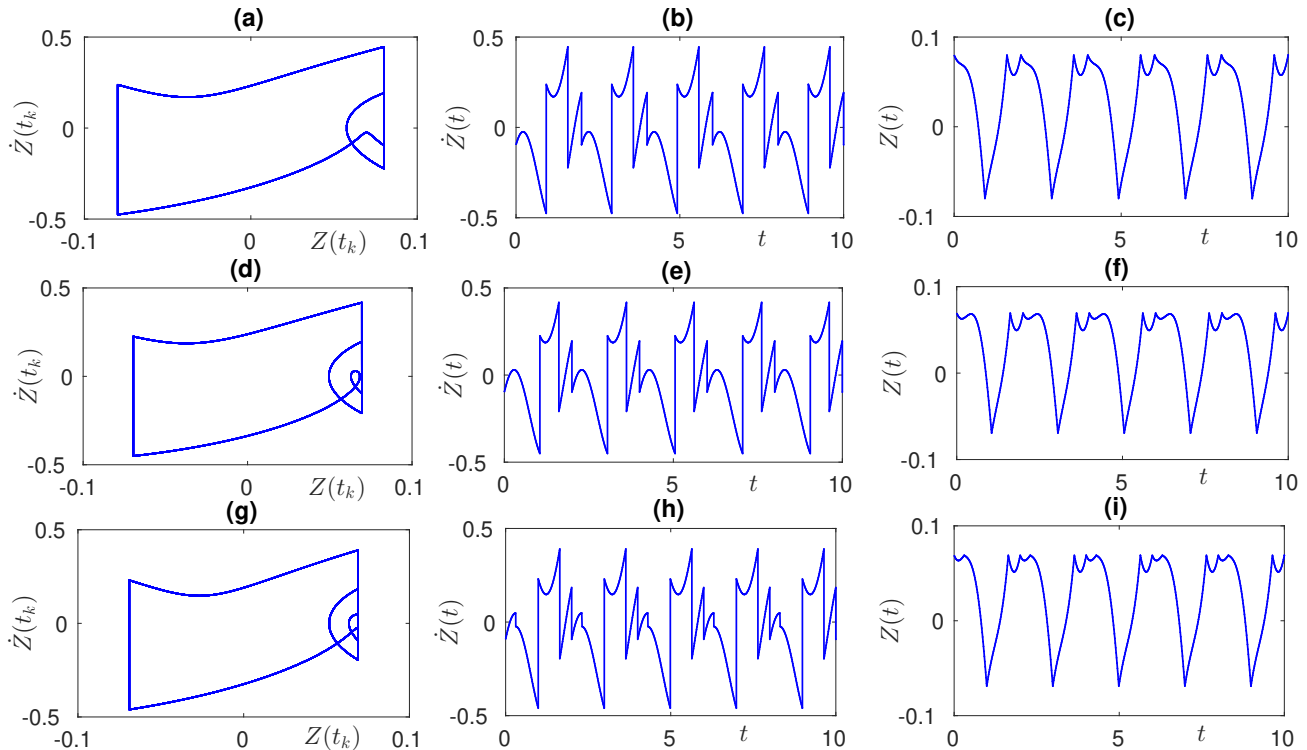


Figure 7: Phase portrait and time series of period-2 motion, with $Z(t_0) = d/2$. (a)-(c) 2:1 motion for $\beta = \pi/6$, $d = 0.16$, $s = 0.27$, $\dot{Z}(t_0) = 0.1924$, $\varphi = 1.015$; (d)-(f) Grazing behavior of 2:1 motion for $\beta = \pi/6$, $d = 0.139$, $s = 0.23$, $\dot{Z}(t_0) = 0.1959$, $\varphi = 0.7788$; (g)-(i) (3:1) motion for $\beta = \pi/6$, $d = 0.138$, $s = 0.23$, $\dot{Z}(t_0) = 0.1845$, $\varphi = 0.7342$. For all figures $M = 124.5$ g, $r = 0.5$, $\|\hat{F}\| = 5$ N and $\omega = 5\pi$ Hz.

4.2 The grazing transition and bistability

For $\beta = \pi/6$ we numerically detect a different type of critical point for the 2:1 period-2 solutions, namely, grazing bifurcations as indicated by the vertical lines at $d = G_1$ and $d = G_2$ in Figure 5 (j)-(l), at which $\dot{Z}_j = 0$ and $Z_j = d/2$ [42, 44, 47]. Figure 8 zooms in on the bifurcation branches near these values. At these values of d there are transitions between 2:1 and 3:1 period-2 motions. The transition from 2:1 to 3:1 period-2 behavior at $d = G_1$ is illustrated by the phase portrait and time series in Figure 7. The initial conditions for these numerical simulations are obtained from the analytical expressions (3.0.15) - (3.0.18). In Figure 7 (d) the transition P_2 takes the form of a loop in the \dot{Z} vs. Z phase plane. As d decreases, the loop intersects with $Z = d/2$, corresponding to an impact on ∂B with $\dot{Z}_j = 0$. For decreasing d this additional impact persists as shown in Figure 7 (d), yielding 3:1 period-2 solutions with an additional P_1 transition prior to P_2 .

Figure 8 compares the grazing bifurcation at $d = G_1$ with a grazing bifurcation that occurs as d increases, leading to a transition from 3:1 to 2:1 period-2 solutions at $d = G_2$. The phase plane behavior for $d = G_1$ and $d = G_2$ are in panels (d) and (g), respectively. In addition, the bi-stability of 3:1 and 2:1 period-2 solutions for $G_1 < d < G_2$ is shown via the bifurcation branches of \dot{Z}_k , φ_k and Δt_k , as well as via

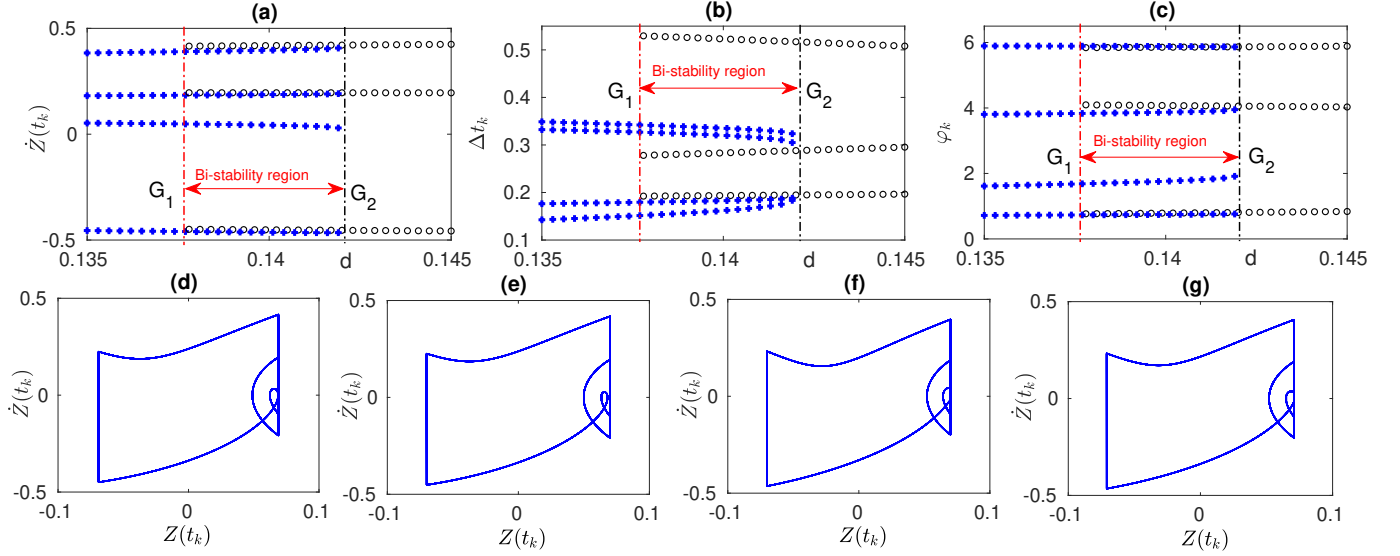


Figure 8: Bistable behavior of periodic 2:1 (black open circles o's) and 3:1 (blue crosses +'s) solutions in the vicinity of the grazing bifurcation $0.1378 < d < 0.1419$ for a) \dot{Z}_k , b) φ_k , c) Δt_k . Phase portraits with $Z(t_0) = d/2$ for d) Grazing point G_1 for $\beta = \pi/6$, $d = 0.1378$, $s = 0.221$, $\dot{Z}(t_0) = 0.416$, $\varphi = 5.842$; e) 2:1 motion for $\beta = \pi/6$, $d = 0.14$, $s = 0.224$, $\dot{Z}(t_0) = 0.4185$, $\varphi = 5.855$; f) 3:1 motion for $\beta = \pi/6$, $d = 0.14$, $s = 0.224$, $\dot{Z}(t_0) = 0.3967$, $\varphi = 5.88$; g) Grazing point G_2 for $\beta = \pi/6$, $d = 0.1419$, $s = 0.228$, $\dot{Z}(t_0) = 0.4069$, $\varphi = 5.864$.

the different phase plane behaviors at a $d = .14$ in this bistable region. While [45] in chapter 6 explores some conditions for grazing and sticking and asymmetric behavior in the case with $\beta = 0$, in general this bi-stability of different n:1 solutions via grazing has not been explored there or in other contexts.

While not the focus of this paper, these results illustrate the importance of grazing bifurcations in driving different types of transitions in the VI-EH, as well as for the potential for hysteresis between bistable behaviors. The analytical conditions for this type of bifurcation in the case of the VI-EH is left for future investigation.

5 Energy output

Here we investigate the output voltage of the 2:1 period-2 behavior and compare these results with the 1:1 period-2 motion published in [55]. Three variables corresponding to output voltage are shown, output voltage $U_k - U_{in}$ at the k^{th} impact, average output per impact \bar{U}_I , and averaged output per unit of time \bar{U}_T . The derivation of $U_k - U_{in}$ is summarized in [54] and \bar{U}_I , \bar{U}_T are defined as

$$\bar{U}_I = \frac{\sum_{k=1}^N (U_k - U_{in})}{N}, \quad \bar{U}_T = \frac{\sum_{k=1}^N (U_k - U_{in})}{t_f - t_0}, \quad (5.0.1)$$

where N is the sample size of impacts and $t_f - t_0 = \frac{\omega}{\pi}(\tau_f - \tau_0)$ is the corresponding non-dimensionalized time interval. We average over this time interval, since it is just a constant rescaling of the dimensionalized

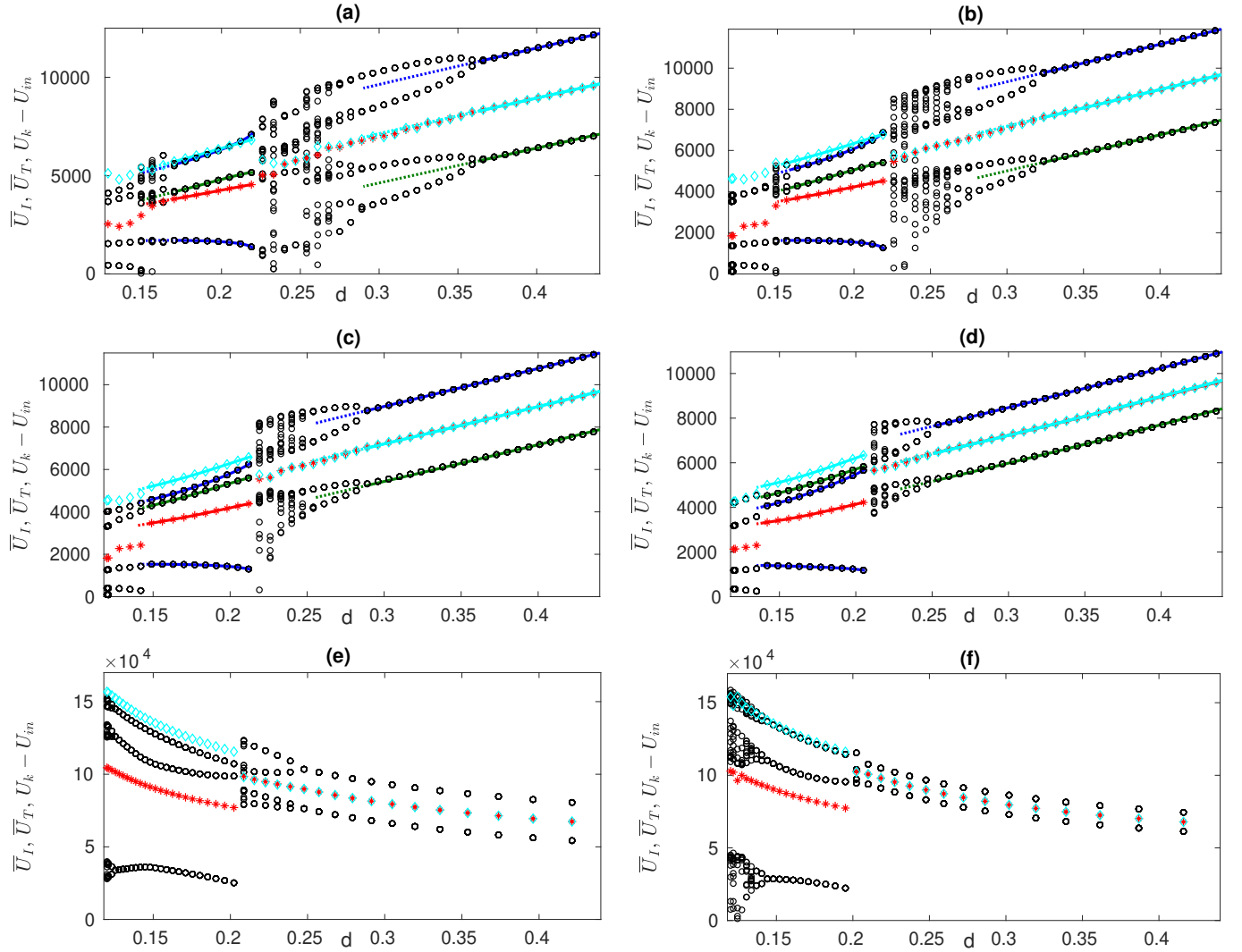


Figure 9: Analytical results (solid and dashed lines) and numerical simulations (open circles o 's, stars $*$'s and diamonds \diamond 's) for output voltage \bar{U}_I (red) and \bar{U}_T (cyan) and $U_k - U_{in}$ for (a) $\beta = \pi/2$, $0.19 < s < 0.72$; (b) $\beta = \pi/3$, $0.19 < s < 0.72$; (c) $\beta = \pi/4$, $0.19 < s < 0.72$; (d) $\beta = \pi/6$, $0.19 < s < 0.72$. For 2:1 period-2 solutions, in (a)-(c) the transitions P_3, P_2, P_1 are located from top to bottom, while in (d), P_2, P_3, P_1 are located from top to bottom. (e) For $\beta = \pi/2$, $s = 0.85$ with varying $\|\hat{F}\|$ between 6 and 22. (f) For $\beta = \pi/6$, $s = 0.85$ with varying $\|\hat{F}\|$ between 6 and 22. For all figures $M = 124.5$ g, $r = 0.5$, $\omega = 5\pi$ Hz.

time interval, and then it is easy to compare \bar{U}_I and \bar{U}_T on the same plot.

Figure 9 shows the output voltage for the 1:1 and 2:1 period-2 regimes, together with period doubled and chaotic regimes between these behaviors, for four different incline angles β . Panels (a)-(d) show variation due to cylinder length s with fixed strength of forcing $\|\hat{F}\|$ and panels (e)-(f) show variations in $\|\hat{F}\|$ with fixed s . One obvious difference is the trend in output voltage, as observed previously in Figure 2. Away from bifurcations, the output voltage increases with both increasing $\|F\|$ and increasing s . Then

in (a)-(d) U_k decreases with d since d is proportional to s , while in (e)-(f) U_k shows a nonlinear increasing trend with decreasing d , due to the inverse relationship $d = \frac{sM\omega^2}{\|\hat{F}\|\pi^2}$ to $\|\hat{F}\|$, as well as in the gravitational term $\bar{g} = \frac{Mg \sin \beta}{\|\hat{F}\|}$.

The bifurcations in the motion also result in changes in the output voltage, which we discuss in terms of the different measures of averaged output voltage. For 1:1 periodic motion, the average energy per impact \bar{U}_I is equal to the average energy per unit of time \bar{U}_T , given that there are exactly two impacts for the 1:1 period-2 solutions. For the period doubled 1:1 solutions, as well as for more complex and chaotic behavior as shown for smaller values of $d > d_{\text{graz}}$, we see a slight increase in the rate of decrease with d of the average output voltage in (a)-(d), due primarily to the combination of values of impact velocities in the period doubled and more complex solutions that include some low velocity impacts. Following the transition to 2:1 period-2 motion for $d < d_{\text{graz}}$ the average energy outputs \bar{U}_I and \bar{U}_T show jumps in the output value. Averaged output per impact \bar{U}_I decreases due to the additional low velocity impact on ∂B in the period $T = 2$ for 2:1 period-2 solution. For the same reason, \bar{U}_T increases due to this additional impact per period of the forcing. Similarly, for the transition from 2:1 period-2 solutions to 3:1 period-2 solutions, the additional low velocity impact results in jumps both in U_I , which decreases across this critical value of d , and in U_T , which increases across this critical transition. Note that here we show only the grazing transition at $d = G_1$ for 2:1 to 3:1 period-2 solutions, corresponding to decreasing d in producing the bifurcation branches.

We also observe differences in the output voltages for different angles β in terms of the location in d and sequence of period doubling bifurcations and complex or chaotic behavior, and for the value of d at which the transition to 2:1 period-2 solutions occurs. In general, as β increases, so do both the value of d at which period doubling of the 1:1 solution occurs, and the value of d_{graz} , the maximum value for 2:1 period-2 solutions. Comparing Panels (a)-(d), for which d decreases with s , and Panels (e)-(f), for which d decreases with increasing $\|\hat{F}\|$, we observe a larger range of d in (a)-(d) for period doubled and complex or chaotic behavior. This is partly due to the fact that even though d decreases with increasing $\|\hat{F}\|$, the coefficient \bar{g} also decreases with increasing $\|\hat{F}\|$. Then for (e)-(f) as d decreases there is a reduced influence of gravity, which would otherwise generate period doubled and complex behavior. For the 1:1 motion there is a small variation of the output voltage (less than 1%) with β , for the maximum over the range of d shown in panels (a)-(d), and similarly if we compare maximum output voltages over 2:1 motions for different angles. However, the parameter values at which these maxima occur differ with the incline β .

The result of this investigation suggests that the choice of the most efficient dynamical regime/device design in terms of the harvested electrical energy depends on the choice of measure for average output voltage and the changes in the parameter values of the system and the forcing.

6 Conclusions

In this paper we determine semi-analytical solutions and stability conditions for the 2:1 period-2 motion of an inclined vibro-impacting energy harvester (VI-EH). These results also provide insight into the VI-EH's energy harvesting potential. The device is composed of a ball moving in a cylinder with dielectric elastomer

(DE) material at the cylinder ends. It is driven by a harmonic forcing, and positioned with an incline angle. Energy is generated through impacts of the ball with the DE material, and the device exhibits $n:m$ motion, where n indicates the number of impacts of the ball with the DE material on the bottom of the cylinder ∂B , and m is the number of impacts on the top ∂T . Semi-analytical expressions for the generic period- T motion are derived through the three nonlinear mappings, that map the motion between the 3 impacts in the 2:1 motion per period. These maps, together with conditions that capture jump discontinuities in the velocity at impact, yield quadruples for the impact velocity, phase shift at impact, time intervals between the impacts. Analytical solutions are in excellent agreement with the numerical ones. Bifurcation points are obtained from a linear stability analysis around asymmetric periodic solutions. Based on the results it can be stated that:

1. For larger values of the incline angle β , the stability behavior of the 2:1 periodic motion exhibits predominance of node stability in the observed range of d . These solutions lose stability through period doubling bifurcation for smaller values of d . This behavior is shown for $\beta = \pi/2$ and $\beta = \pi/3$.

2. For smaller values of incline β , the transition from 2:1 periodic behavior to 3:1 periodic behavior was observed as d decreases. This transition occurs via a grazing bifurcation that is numerically detected. It occurs for larger values of d compared with the values for other instabilities predicted by the linear analysis. These results are shown for $\beta = \pi/6$, for which bi-stability of the 2:1 and 3:1 solutions is numerically demonstrated near grazing.

3. The periodic asymmetric motions are less efficient compared to the motion with alternating top and bottom impacts per period of the forcing, when measured in terms of converted electrical energy per impact.

4. The 2:1 periodic motion results in significant differences between the two measures of the harvested energy, averaged per impact, U_I , and averaged over time interval, U_T , giving greater value for U_T . Similar observations for 3:1 behavior are also shown.

A Appendix

Here we give the details for the calculations of the eigenvalues $\lambda_{1,2}$. The entries in the matrices in (4.1.2) are

$$\begin{aligned} \frac{\partial t_{k+1}}{\partial t_k} &= \frac{r\dot{Z}_k - \bar{g}T_1 - f(t_k)T_1}{r\dot{Z}_k - \bar{g}T_1 - F_1(t_{k+1}) + F_1(t_k)}, \\ \frac{\partial t_{k+1}}{\partial \dot{Z}_k} &= \frac{-rT_1}{r\dot{Z}_k - \bar{g}T_1 - F_1(t_{k+1}) + F_1(t_k)}, \\ \frac{\partial \dot{Z}_{k+1}}{\partial t_k} &= \frac{\partial t_{k+1}}{\partial t_k} [f(t_{k+1}) + \bar{g}] - [f(t_k) + \bar{g}], \\ \frac{\partial \dot{Z}_{k+1}}{\partial \dot{Z}_k} &= -r + \frac{\partial t_{k+1}}{\partial \dot{Z}_k} [f(t_{k+1}) + \bar{g}], \end{aligned} \tag{A.0.1}$$

$$\begin{aligned}
\frac{\partial t_{k+2}}{\partial t_{k+1}} &= \frac{r\dot{Z}_{k+1} - \bar{g}T_2 - f(t_{k+1})T_2}{r\dot{Z}_{k+1} - \bar{g}T_2 - F_1(t_{k+2}) + F_1(t_{k+1})}, \\
\frac{\partial t_{k+2}}{\partial \dot{Z}_{k+1}} &= \frac{-rT_2}{r\dot{Z}_{k+1} - \bar{g}T_2 - F_1(t_{k+2}) + F_1(t_{k+1})}, \\
\frac{\partial \dot{Z}_{k+2}}{\partial t_{k+1}} &= \frac{\partial t_{k+2}}{\partial t_{k+1}} [f(t_{k+2}) + \bar{g}] - [f(t_{k+1}) + \bar{g}], \\
\frac{\partial \dot{Z}_{k+2}}{\partial \dot{Z}_{k+1}} &= -r + \frac{\partial t_{k+2}}{\partial \dot{Z}_{k+1}} [f(t_{k+2}) + \bar{g}],
\end{aligned} \tag{A.0.2}$$

and

$$\begin{aligned}
\frac{\partial t_{k+3}}{\partial t_{k+2}} &= \frac{r\dot{Z}_{k+2} - \bar{g}T_3 - f(t_{k+2})T_3}{r\dot{Z}_{k+2} - \bar{g}T_3 - F_1(t_{k+3}) + F_1(t_{k+2})}, \\
\frac{\partial t_{k+3}}{\partial \dot{Z}_{k+2}} &= \frac{-rT_3}{r\dot{Z}_{k+2} - \bar{g}T_3 - F_1(t_{k+3}) + F_1(t_{k+2})}, \\
\frac{\partial \dot{Z}_{k+3}}{\partial t_{k+2}} &= \frac{\partial t_{k+3}}{\partial t_{k+2}} [f(t_{k+3}) + \bar{g}] - [f(t_{k+2}) + \bar{g}], \\
\frac{\partial \dot{Z}_{k+3}}{\partial \dot{Z}_{k+2}} &= -r + \frac{\partial t_{k+3}}{\partial \dot{Z}_{k+2}} [f(t_{k+3}) + \bar{g}].
\end{aligned} \tag{A.0.3}$$

For the period-2 motion the trace of the linearized matrix DP are

$$Tr(DP) = -\frac{r^6 \dot{Z}(t_k)}{F_1(t_{k+2}) - F_1(t_{k+3}) - rF_1(t_{k+1}) + rF_1(t_{k+2}) + r^2F_1(t_k) - r^2F_1(t_{k+1}) + \sigma_1}, \tag{A.0.4}$$

where $\sigma_1 = r^3\dot{Z}(t_k) - \bar{g}T_3 + r\bar{g}T_2 - r^2\bar{g}T_1$. The determinant of the linearized matrix DP is a nonlinear function of $r, \bar{g}, \dot{Z}(t_k), T_1, T_2, T_3, f(t_k), f(t_{k+1}), f(t_{k+2}), f(t_{k+3}), F_1(t_k), F_1(t_{k+1}), F_1(t_{k+2})$ and $F_1(t_{k+3})$.

References

- [1] N. G. Stephen, "On energy harvesting from ambient vibration," *Journal of Sound and Vibration*, 2006.
- [2] C. R. Bowen, V. Y. Topolov, and H. A. Kim, *Modern Piezoelectric Energy-Harvesting Materials*. 2016.
- [3] D. Briand, E. Yeatman, and S. Roundy, *Micro Energy Harvesting*. 2015.
- [4] B. Yang, H. Liu, J. Liu, and C. Lee, *Micro and Nano Energy Harvesting Technologies*. 2014.
- [5] N. Elvin and A. Erturk, *Advances in energy harvesting methods*. 2013.

- [6] M. Wiercigroch, A. Najdecka, and V. Vaziri, “Nonlinear dynamics of pendulums system for energy harvesting,” in *Springer Proceedings in Physics*, 2011.
- [7] K. Kecik and M. Borowiec, “An autoparametric energy harvester,” *European Physical Journal: Special Topics*, 2013.
- [8] Y. Jia, J. Yan, K. Soga, and A. A. Seshia, “Parametric resonance for vibration energy harvesting with design techniques to passively reduce the initiation threshold amplitude,” *Smart Materials and Structures*, 2014.
- [9] R. V. Bobryk and D. Yurchenko, “Enhancing energy harvesting by a linear stochastic oscillator,” *Probabilistic Engineering Mechanics*, 2016.
- [10] R. V. Bobryk and D. Yurchenko, “On enhancement of vibration-based energy harvesting by a random parametric excitation,” *Journal of Sound and Vibration*, 2016.
- [11] K. Yerrapragada, M. H. Ansari, and M. A. Karami, “Enhancing power generation of floating wave power generators by utilization of nonlinear roll-pitch coupling,” *Smart Materials and Structures*, 2017.
- [12] D. Yurchenko and P. Alevras, “Parametric pendulum based wave energy converter,” *Mechanical Systems and Signal Processing*, 2018.
- [13] F. E. Dotti and M. D. Sosa, “Pendulum systems for harvesting vibration energy from railroad tracks and sleepers during the passage of a high-speed train: A feasibility evaluation,” *Theoretical and Applied Mechanics Letters*, 2019.
- [14] Y. Kuang and M. Zhu, “Parametrically excited nonlinear magnetic rolling pendulum for broadband energy harvesting,” *Applied Physics Letters*, 2019.
- [15] R. H. Avançaço, A. M. Tusset, M. Suetake, H. A. Navarro, J. M. Balthazar, and A. Nabarrete, “Energy harvesting through pendulum motion and DC generators,” *Latin American Journal of Solids and Structures*, 2019.
- [16] Z. Ghouli, M. Hamdi, F. Lakrad, and M. Belhaq, “Quasiperiodic energy harvesting in a forced and delayed Duffing harvester device,” *Journal of Sound and Vibration*, 2017.
- [17] N. Lingala, N. Sri Namachchivaya, I. Pavlyukevich, and H. C. Yeong, “Periodically Forced Noisy Mathieu-Duffing-Van der Pol Oscillator: From Energy Harvesting to Stochastic Resonance,” tech. rep., 2015.
- [18] H. T. Zhu, “Probabilistic solution of a duffing-type energy harvester system under Gaussian white noise,” *ASCE-ASME Journal of Risk and Uncertainty in Engineering Systems, Part B: Mechanical Engineering*, 2015.
- [19] D. D. Quinn, A. L. Triplett, A. F. Vakakis, and L. A. Bergman, “Energy harvesting from impulsive loads using intentional essential nonlinearities,” *Journal of Vibration and Acoustics, Transactions of the ASME*, 2011.

- [20] G. Sebald, H. Kuwano, D. Guyomar, and B. Ducharne, “Experimental Duffing oscillator for broadband piezoelectric energy harvesting,” *Smart Materials and Structures*, 2011.
- [21] P. L. Green, K. Worden, K. Atallah, and N. D. Sims, “The benefits of Duffing-type nonlinearities and electrical optimisation of a mono-stable energy harvester under white Gaussian excitations,” *Journal of Sound and Vibration*, 2012.
- [22] M. F. Daqaq, R. Masana, A. Erturk, and D. D. Quinn, “On the role of nonlinearities in vibratory energy harvesting: A critical review and discussion,” 2014.
- [23] S. P. Pellegrini, N. Tolou, M. Schenk, and J. L. Herder, “Bistable vibration energy harvesters: A review,” in *Journal of Intelligent Material Systems and Structures*, 2013.
- [24] Y. Gao, Y. Leng, A. Javey, D. Tan, J. Liu, S. Fan, and Z. Lai, “Theoretical and applied research on bistable dual-piezoelectric-cantilever vibration energy harvesting toward realistic ambience,” *Smart Materials and Structures*, 2016.
- [25] H. Fu and E. M. Yeatman, “Rotational energy harvesting using bi-stability and frequency up-conversion for low-power sensing applications: Theoretical modelling and experimental validation,” *Mechanical Systems and Signal Processing*, 2019.
- [26] D. H. Hawes and R. S. Langley, “Limits on the power available to harvest from broadband random excitation,” *Journal of Sound and Vibration*, 2017.
- [27] S. Zhou and L. Zuo, “Nonlinear dynamic analysis of asymmetric tristable energy harvesters for enhanced energy harvesting,” *Communications in Nonlinear Science and Numerical Simulation*, 2018.
- [28] D. Huang, S. Zhou, and G. Litak, “Analytical analysis of the vibrational tristable energy harvester with a RL resonant circuit,” *Nonlinear Dynamics*, 2019.
- [29] H. Deng, Y. Du, Z. Wang, J. Ye, J. Zhang, M. Ma, and X. Zhong, “Poly-stable energy harvesting based on synergetic multistable vibration,” *Communications Physics*, 2019.
- [30] T. Yang and Q. Cao, “Novel multi-stable energy harvester by exploring the benefits of geometric nonlinearity,” *Journal of Statistical Mechanics: Theory and Experiment*, 2019.
- [31] A. Abdelkefi, A. H. Nayfeh, and M. R. Hajj, “Modeling and analysis of piezoaeroelastic energy harvesters,” *Nonlinear Dynamics*, 2012.
- [32] J. Wang, G. Li, S. Zhou, and G. Litak, “Enhancing wind energy harvesting using passive turbulence control devices,” *Applied Sciences (Switzerland)*, 2019.
- [33] J. Wang, S. Zhou, Z. Zhang, and D. Yurchenko, “High-performance piezoelectric wind energy harvester with Y-shaped attachments,” *Energy Conversion and Management*, 2019.
- [34] Z. Jin, G. Li, J. Wang, and Z. Zhang, “Design, modeling, and experiments of the vortex-induced vibration piezoelectric energy harvester with bionic attachments,” *Complexity*, 2019.

- [35] S. Orrego, K. Shoele, A. Ruas, K. Doran, B. Caggiano, R. Mittal, and S. H. Kang, “Harvesting ambient wind energy with an inverted piezoelectric flag,” *Applied Energy*, 2017.
- [36] R. A. Ibrahim, “Vibro-impact dynamics: Modeling, mapping and applications,” *Lecture Notes in Applied and Computational Mechanics*, 2009.
- [37] M. F. Dimentberg and D. V. Iourtchenko, “Random vibrations with impacts: A review,” 2004.
- [38] A. B. Nordmark, “Universal limit mapping in grazing bifurcations,” *Physical Review E - Statistical Physics, Plasmas, Fluids, and Related Interdisciplinary Topics*, 1997.
- [39] D. R. Chillingworth, “Discontinuity geometry for an impact oscillator,” *Dynamical Systems*, 2002.
- [40] D. J. Wagg and S. R. Bishop, “Dynamics of a two degree of freedom vibro-impact system with multiple motion limiting constraints,” *International Journal of Bifurcation and Chaos in Applied Sciences and Engineering*, 2004.
- [41] D. J. Wagg, “Periodic sticking motion in a two-degree-of-freedom impact oscillator,” *International Journal of Non-Linear Mechanics*, 2005.
- [42] D. J. Simpson, S. J. Hogan, and R. Kuske, “Stochastic regular grazing bifurcations,” *SIAM Journal on Applied Dynamical Systems*, 2013.
- [43] P. Kumar, S. Narayanan, and S. Gupta, “Stochastic bifurcations in a vibro-impact DuffingVan der Pol oscillator,” *Nonlinear Dynamics*, 2016.
- [44] M. Di Bernardo, C. J. Budd, A. R. Champneys, and P. Kowalczyk, “Piecewise-smooth dynamical systems theory and applications,” in *Applied Mathematical Sciences (Switzerland)*, 2008.
- [45] A. C. Luo and Y. Guo, *Vibro-Impact Dynamics*. 2013.
- [46] A. C. Luo, “Period-doubling induced chaotic motion in the LR model of a horizontal impact oscillator,” *Chaos, Solitons and Fractals*, 2004.
- [47] D. J. W. Simpson and R. Kuske, “The influence of localized randomness on regular grazing bifurcations with applications to impacting dynamics,” *JVC/Journal of Vibration and Control*, 2018.
- [48] S. W. Shaw and P. J. Holmes, “A periodically forced piecewise linear oscillator,” *Journal of Sound and Vibration*, 1983.
- [49] A. El Aroudi, H. Ouakad, L. Benadero, and M. Younis, “Analysis of bifurcation behavior of a piecewise linear vibrator with electromagnetic coupling for energy harvesting applications,” *International Journal of Bifurcation and Chaos*, 2014.
- [50] M. Borowiec, G. Litak, and S. Lenci, “Noise effected energy harvesting in a beam with stopper,” *International Journal of Structural Stability and Dynamics*, 2014.
- [51] O. V. Gendelman and A. Alloni, “Dynamics of forced system with vibro-impact energy sink,” *Journal of Sound and Vibration*, 2015.

- [52] B. D. Truong, C. Phu Le, and E. Halvorsen, “Power optimization and effective stiffness for a vibration energy harvester with displacement constraints,” *Journal of Micromechanics and Microengineering*, 2016.
- [53] M. Bendame, E. Abdel-Rahman, and M. Soliman, “Wideband, low-frequency springless vibration energy harvesters: Part i,” *Journal of Micromechanics and Microengineering*, 2016.
- [54] D. Yurchenko, Z. H. Lai, G. Thomson, D. V. Val, and R. V. Bobryk, “Parametric study of a novel vibro-impact energy harvesting system with dielectric elastomer,” *Applied Energy*, 2017.
- [55] L. Serdukova, R. Kuske, and D. Yurchenko, “Stability and bifurcation analysis of the period-T motion of a vibroimpact energy harvester,” *Nonlinear Dynamics*, 2019.